JGR Solid Earth

RESEARCH ARTICLE
10.1029/2020JB019896

Key Points:
- A new probabilistic geodynamic modeling approach is presented to tighten existing constraints on olivine rheology
- Radial anisotropy beneath the Pacic plate provides an important constraint on mantle rheology
- Our analysis reinforces the possibility of strong shear flow beneath the Pacific plate

Supporting Information:
- Supporting Information S1

Correspondence to:
C. Jain,
chhavi.jain@wustl.edu

Citation:
Jain, C., & Korenaga, J. (2020). Synergy of experimental rock mechanics, seismology, and geodynamics reveals still elusive upper mantle rheology. *Journal of Geophysical Research: Solid Earth*, *125*, e2020JB019896. https://doi.org/10.1029/2020JB019896

Received 2 APR 2020
Accepted 6 NOV 2020
Accepted article online 12 NOV 2020

Synergy of Experimental Rock Mechanics, Seismology, and Geodynamics Reveals Still Elusive Upper Mantle Rheology

Chhavi Jain[1,2] **and Jun Korenaga**[1]

[1]Department of Earth and Planetary Sciences, Yale University, New Haven, CT, USA, [2]Department of Earth and Planetary Sciences, Washington University in St. Louis, St. Louis, MO, USA

Abstract We present a novel geodynamic approach that can potentially tighten existing constraints on mantle rheology. This new approach, which we call probabilistic geodynamic modeling, is applied here to the rheology of the upper mantle. We combine the numerical modeling of plate-driven corner flow and the seismic observation of radial anisotropy, aiming to reduce substantial uncertainties associated with experimentally derived flow laws, but our results also highlight the complex competition among different deformation mechanisms under mantle conditions. Despite the remaining rheological uncertainty, our study suggests that significant background shear flow is required near the lithosphere-asthenosphere boundary to explain the strong radial anisotropy observed at 100–200 km depth underneath the Pacific plate, and the plausible nature of this background flow is characterized using our new probabilistic approach. Our analysis also provides a new insight into the asthenospheric water content and the grain size distribution in the upper mantle, but these results are also subject to nontrivial nonuniqueness. The merit of our probabilistic approach lies in its ability to assess the extent of such nonuniqueness, and we demonstrate this by quantifying the robustness of some of our results.

Plain Language Summary A detailed understanding of how silicate minerals deform under various conditions is central to conducting realistic simulations of mantle dynamics, but the currently available experimental constraints on the flow laws of olivine, which is the dominant phase of the upper mantle, suffer from considerable uncertainties. We present a new kind of geodynamic modeling, which can reduce such uncertainties by assimilating geophysical observations. Unlike previous similar attempts, our approach properly handles parameter uncertainties such that the flow laws under consideration remain consistent with experimental deformation data. Most important, our new approach provides a unifying framework to combine experimental rock mechanics, observational geophysics, and theoretical geodynamics in a self-consistent manner.

1. Introduction

The knowledge of upper mantle rheology is crucial to our understanding of mantle convection and related tectonic processes that have shaped our environment. Because olivine is the most abundant and usually the weakest phase in the upper mantle (Karato & Wu, 1993), the rheology of olivine aggregates is considered to be representative of upper mantle rheology. Olivine primarily deforms by diffusion and dislocation creep mechanisms, and flow laws for these mechanisms have often been used to implement geodynamic models (e.g., Kneller et al., 2005; Rose & Korenaga, 2011; Zhong & Gurnis, 1996). Flow law parameters for these mechanisms are usually obtained from experimental deformation data of olivine aggregates. Because both diffusion and dislocation creep operate in parallel, however, delineating these two mechanisms from experimental data has been difficult. Our recent reanalysis of existing experimental data using a rigorous statistical framework, implemented by Markov chain Monte Carlo (MCMC) sampling, has revealed that, owing to the highly nonlinear nature of parameter estimation as well as large data uncertainties, some flow law parameters are only poorly constrained (Jain et al., 2018, 2019). If these experimentally constrained flow laws are applied directly in geodynamic modeling, their uncertainties would yield too wide a range of viscosity predictions to be useful. To design more realistic and reliable mantle dynamic models; therefore, it is necessary to improve existing constraints on olivine rheology.

Whereas experimental rock mechanics provides direct estimates on olivine rheology, additional constraints may be obtained from some geophysical observations. Olivine rheology influences many properties of the lithosphere and the upper mantle, such as seismic anisotropy and attenuation, convection planform, heat transport to the surface, and lithospheric flexure. Consequently, geophysical observations of these phenomena may be used to draw some inferences on upper mantle rheology.

Some previous studies have indeed used geophysical data to constrain flow law parameters for olivine rheology. The most straightforward approach to conduct geophysical inversion is to run multiple forward geodynamic models assuming different rheological parameters for the upper mantle. The subset of parameters that yield the smallest misfits to geophysical data may provide useful constraints on the flow law parameters for olivine rheology. A number of studies have implemented this approach with different geodynamical settings (e.g., Lee et al., 2011; van Hunen et al., 2005; Watts & Zhong, 2000). In particular, Alisic et al. (2012) tested a range of values for the stress exponent of dislocation creep in their global mantle flow model and compared their results with surface observables, such as plate velocity and the angle of subducting plates. The stress exponent was varied between 2 and 3.75 to explore the entire range of values previously suggested for this parameter by experiment studies. Because each geodynamic simulation is time-consuming, only a few parameter values could be tested. Consequently, the uncertainty in the inversion result is difficult to assess.

Recently, Baumann and Kaus (2015) presented a more intensive geodynamic inversion scheme based on Bayesian statistics, in which a diverse set of data, including topography, gravity, and surface velocity measurements, were simultaneously used to constrain all the flow law parameters for dislocation creep. A range of laboratory-derived estimates on the flow law parameters served as a priori bounds within which each parameter was allowed to vary. The multidimensional model space so defined was finely explored with the help of MCMC sampling. Approximately 2×10^6 forward models were conducted, and the resulting a posteriori probability distributions were used to determine the optimum values of all flow law parameters and the associated uncertainty. Despite its high computational cost, this approach allows for an exhaustive search of the multidimensional model domain and also provides a way to account for uncertainties in geophysical data.

Worthen et al. (2014) suggested a computationally less expensive, adjoint-based inversion method that uses surface plate velocities as constraints to estimate the flow law parameters for dislocation creep in olivine. Instead of sampling a range of values for the unknown flow law parameters, the adjoint-based approach iteratively solves for the minimum in the cost or the misfit function and computes the gradients of the cost function to guide its search for the "best fit" solution. This reduces the number of iterations needed to reach a convergent solution. Li et al. (2017) made improvements to the adjoint-based inversion technique and elucidated its application by modeling time-dependent mantle convection with nonlinear rheology. Their inversion scheme could successfully reproduce the expected values of the stress exponent and the scalar coefficient for dislocation creep in the upper mantle. However, it is difficult to assess the efficiency and the success of the technique in the case where more realistic mantle rheologies, such as a composite flow law with both diffusion and dislocation creep, are assumed and all the flow law parameters, including the activation energies and volumes, are inverted for. Moreover, in these studies, little importance is given to laboratory-derived estimates on the flow law parameters. Even though experimental results are associated with large uncertainties, they are nonetheless the most direct measure of olivine rheology, and it would be beneficial for a geophysical inversion scheme to give some weightage to this information. For example, the adjoint-based inversion scheme of Ratnaswamy et al. (2015) has a provision to incorporate this information as a priori knowledge.

Yet another approach to geophysical inversion was presented by Yang and Gurnis (2016). Here, the radial and lateral viscosity variation in the mantle were investigated based on the observations of long-wavelength geoid, free-air gravity anomaly, gravity gradients, and residual topography. The Powell's method (Press et al., 2007) was used to invert for a radial viscosity profile as well as the activation energy for diffusion creep. It iteratively searches for the minimum of the cost function but does not rely on gradients to guide the search, making it computationally less expensive than the adjoint-based method. However, the inversion is repeated with different initial guesses and searching orders to avoid falling into a local minimum. The total number of iterations required to ensure convergence also increases with the number of unknown

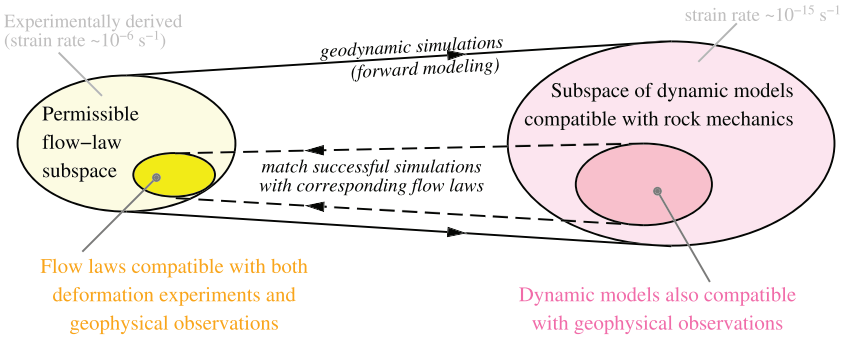

Figure 1. Schematic diagram to demonstrate our probabilistic geodynamic modeling scheme.

parameters. The efficiency of this method may, therefore, be impacted if more complex and realistic rheologies are assumed.

Whereas each of the aforementioned geophysical inversion technique has its merits and demerits, all of them share one important drawback. These studies overlooked possible correlation between model parameters, for example, covariance between the stress exponent and the activation energy, or the preexponential factor. By ignoring the covariance between parameters, the flow laws tested in these studies are unlikely to be consistent with experimental deformation data. Moreover, the a priori parameter ranges used in these inversions were not directly experimentally derived, which could worsen the compatibility of their results with laboratory data. For example, Baumann and Kaus (2015) simply compiled previously published values for each flow law parameter and used the minimum and the maximum values to define the a priori range. Each prior was further assumed to be normally distributed about the mean of this range. Such a setup for the priors ignores possible inconsistencies between the estimates reported by the different studies and the errors in their inversion results. By realistically accounting for the uncertainties of all model parameters and including covariances, we present here a more effective method to integrate the fields of experimental rock mechanics, observational geophysics, and theoretical geodynamics.

In this study, we propose a new technique, named "probabilistic geodynamic modeling," that aims to tighten existing experimental constraints on flow law parameters via geodynamic modeling. It is implemented as follows (Figure 1). The uncertainties of our composite rheological model (i.e., the combination of diffusion and dislocation creep; Equation 6), derived from global MCMC inversion of experimental data (Jain et al., 2019), are exploited to construct a range of permissible flow laws. By taking the covariance between the parameters into account, we ensure that all of the "perturbed" flow laws are consistent with experimental deformation data. Geodynamic models implemented with such different realizations of the composite flow law could produce disparate dynamic results, only some of which may be consistent with geophysical observations, and if so, the corresponding subset of perturbed flow laws defines new and tighter constraints on olivine rheology.

We demonstrate our new approach by modeling radial anisotropy beneath an oceanic plate. Predictions of seismic anisotropy in the upper mantle have been shown to be sensitive to the assumed viscosity distribution (e.g., Podolefsky et al., 2004), with a composite rheology model yielding a better fit to the observed data on radial anisotropy and surface plate motion than a purely radial viscosity profile (Becker, 2006; Becker et al., 2008). Based on these results, we use tomographic data on radial anisotropy beneath the Pacific plate to constrain flow law parameters for the composite rheology of olivine.

The structure of this paper is as follows. The next section explains our new probabilistic geodynamic modeling approach with detailed stepwise implementation. Our rheological and geodynamic models are also fully described. Next, we will present the seismically derived radial anisotropy structure beneath the Pacific plate. Our predictions of radial anisotropy will be compared against these seismic data. Finally, we will discuss the results of our modeling effort with different assumptions on the water content, the grain sizes, and shear flow in the upper mantle and delineate the set of flow laws and model assumptions that yield realistic estimates on radial anisotropy. We will conclude with a brief discussion on the geodynamic significance of our findings and the prospects of our probabilistic modeling approach.

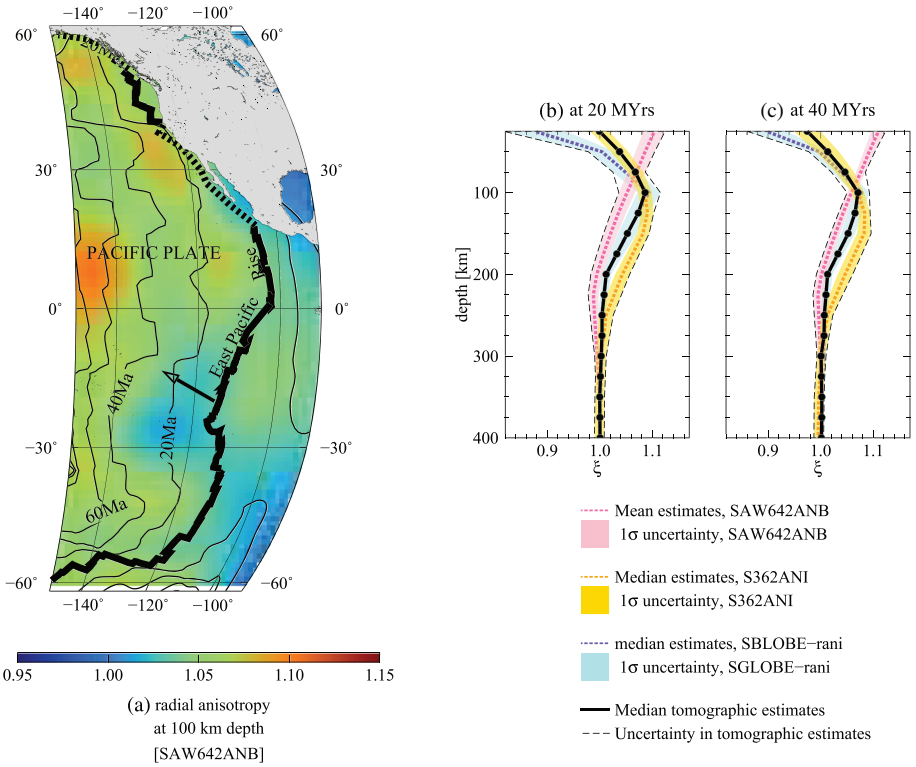

Figure 2. Seismic estimates on radial anisotropy beneath the Pacific plate. Panel (a) presents the distribution of radial anisotropy (ξ) estimated by the tomography model of Panning et al. (2010) at a depth of 100 km below the ocean floor. The thick black line denotes the mid-ocean ridge (East Pacific Rise), and the motion of Pacific plate is indicated by arrow. Thin lines denote isochrons at an interval of 20 Myr. Smallest values of the ξ parameter are in blue and highest in red (colorbar). At a given depth section, radial anisotropy varies along each isochron and across different ages. Panels (b) and (c) represent the depth variation of radial anisotropy, averaged over isochron, for three tomography models: SAW642ANB (Panning et al., 2010, in pink), S362ANI (Moulik & Ekström, 2014, in yellow), and SGLOBE-rani (Chang et al., 2015, in blue), at lithospheric age of (b) 20 Myr and (c) 40 Myr. Each dotted line represents mean estimates on the radial anisotropy parameter, ξ, suggested by a particular tomography model, and the enclosing shaded region denotes the associated 1σ uncertainty. Solid black line denotes the median of the three tomographic estimates, using data at depth intervals of 25 km (solid circles), and black dashed lines delineate the total uncertainty in the median tomographic estimates.

2. Method and Data

2.1. Overview of the Probabilistic Geodynamic Modeling Approach

To illustrate the implementation and range of applications of our new probabilistic geodynamic modeling approach, we choose to model radial anisotropy in the upper mantle beneath the Pacific plate as a representative example. Our two-dimensional geodynamic model extends vertically to a depth of 400 km and laterally to a distance of 6,000 km (corresponding to seafloor age of ~85 Myr) from the ridge axis (zero-age seafloor). By prescribing a surface velocity of 7 cm yr^{-1}, which is appropriate for the Pacific plate (Müller et al., 2008), we simulate steady-state surface-driven corner flow beneath the East Pacific Rise. Upper mantle viscosity is modeled by a composite flow law [Equation 6] for olivine (Jain et al., 2019). Dry flow laws are used to predict viscosity in the lithosphere and wet flow laws in the underlying asthenosphere. Further details on our rheological and geodynamic models are given in sections 2.2 and 2.3. The evolution of radial anisotropy in our model domain is governed by the strain rate field, the velocity gradient field, and the spatial variation of the dominant deformation mechanism, all of which are provided by our corner flow simulation.

Shearing of intrinsically anisotropic minerals, such as olivine and orthopyroxene, along convective flows in the dislocation creep regime causes the reorientation of their crystallographic axes. For the A- and the E-type fabrics expected in the lithosphere and the asthenosphere respectively, the seismic fast axis in olivine, that is, the [100] or the *a* axis, tends to align subparallel to the direction of flow (e.g., Karato et al., 2008; Nicolas & Christensen, 1987). Consequently, the horizontally polarized shear wave is usually faster than

the vertically polarized wave in regions of horizontal spreading whereas the converse is true in regions of vertical flow, for example, beneath the mid-ocean ridge. The radial anisotropy parameter for shear waves, denoted by ξ, is defined as the squared ratio of the velocities of horizontally and vertically polarized waves, V_{SH} and V_{SV}, respectively, that is, $\xi = \left(V_{SH}/V_{SV}\right)^2$. We use the D-Rex code (Kaminski et al., 2004) to model lattice-preferred orientation and derive estimates on the strength of radial anisotropy. Some assumptions associated with our use of the D-Rex code are described in section 2.4. Each perturbed realization of the composite flow law (section 2.2.2) results in a distinct flow simulation and thus a different prediction for radial anisotropy.

Our predictions for radial anisotropy corresponding to an ensemble of perturbed flow laws are compared with surface and body wave tomography models of radial anisotropy beneath the Pacific plate. Seismic data suggest that radial anisotropy varies with depth and lithospheric age. For example, Figure 2a presents the lateral variation of the radial anisotropy parameter according to the model of Panning et al. (2010) at a depth of 100 km. At the given depth, the value of the radial anisotropy parameter ξ appears to vary with the age of the ocean floor and along individual isochrons. For simplicity, we compare our model predictions with seismic data for the top 400 km of the upper mantle at plate ages of 20 and 40 Myr. For this comparison, we use three tomography models: SAW642ANB (Panning et al., 2010), S362ANI (Moulik & Ekström, 2014), and SGLOBE-rani (Chang et al., 2015). At certain depths, however, these models provide very different values of the radial anisotropy parameter (Figures 2b and 2c). Goodness of fit of our model predictions is, therefore, assessed with respect to the median of these models. Figure S1 in the supporting information provides an example of the strain rate and velocity fields predicted by our corner flow model with one set of flow law parameters. The spatial distribution of the regions where dislocation creep dominates is also shown. Using these outputs, the radial anisotropy profile predicted by the D-Rex code at 20 and 40 Myr (Figure S1c) is compared with tomographic models.

Model misfits are evaluated using the χ^2 function defined below:

$$\chi^2\left(t, \{q_k\}\right) = \sum_{i=1}^{N} \frac{\left[\xi_{obs}(i,t) - \xi_{pred}\left(i, t, \{q_k\}\right)\right]^2}{\sigma_{obs}^2(i,t)}. \quad (1)$$

Here $\xi_{obs}(i,t)$ denotes the value of the radial anisotropy parameter given by tomography at the i^{th} point in depth under the oceanic plate of age t, whereas $\xi_{pred}\left(i, t, \{q_k\}\right)$ denotes a corresponding value predicted by our geodynamic model with the $\{q_k\}$ set of perturbed flow law parameters. The difference between them is calculated at 16 depth intervals that span the vertical extent of the model domain, that is, $N = 16$. For a given age, $\chi^2\left(t, \{q_k\}\right)$ is a measure of the total discrepancy between the expected and predicted values of the ξ parameter, normalized by the uncertainty in the tomography models, $\sigma_{obs}(i,t)$ (section 2.5). The subset of all trial models that produce small misfits with tomography are chosen to define new constraints on the flow law parameters of olivine. Ideally, models with $\chi^2/N < 1$ are preferable, but we extend this threshold to 1.3, given the possibility that uncertainties in tomography are underestimated. The mean and standard deviation of the set of acceptable flow laws may serve as the new constraints on olivine rheology. Note here that this implicitly assumes that the successful flow law parameters are normally distributed, which may not always be the case, especially if only a few models yield acceptably small misfits. For a larger set of successful models, more rigorous statistical analysis may be possible based on a posteriori probability distributions of the resultant flow law parameters. As this study is the first demonstration of the probabilistic geodynamic modeling approach, however, we will simply summarize our results here in the form of the mean and the standard deviation of the successful set of flow law parameters.

The pattern of radial anisotropy is strongly influenced by the magnitude of strain produced by dislocation creep that is accumulated along a streamline and by the direction of flow. The composite flow law, our geodynamic and anisotropy models, and the seismic data used to constrain olivine rheology in this study are described in more detail below.

2.2. Our Composite Rheological Model

2.2.1. Constitutive Equations for Olivine Rheology

We model upper mantle rheology in our geodynamic model using a composite flow law for olivine, which assumes the simultaneous operation of both diffusion and dislocation creep under mantle conditions. Dislocation-accommodated grain boundary sliding is not included in the composite flow law because its

contribution is likely to be trivial under upper mantle conditions (Jain et al., 2019). The following constitutive equations govern diffusion and dislocation creep in olivine (Karato, 2008):

$$\dot{\epsilon}_{diff,\,dry} = \dot{\epsilon}_1 = A_1 d^{-p_1} \sigma \exp\left(-\frac{E_1 + PV_1}{RT}\right), \tag{2}$$

$$\dot{\epsilon}_{diff,\,wet} = \dot{\epsilon}_2 = A_2 d^{-p_2} C_w^{r_2} \sigma \exp\left(-\frac{E_2 + PV_2}{RT}\right), \tag{3}$$

$$\dot{\epsilon}_{disl,\,dry} = \dot{\epsilon}_3 = A_3 \sigma^{n_3} \exp\left(-\frac{E_3 + PV_3}{RT}\right), \tag{4}$$

$$\dot{\epsilon}_{disl,\,wet} = \dot{\epsilon}_4 = A_4 \sigma^{n_4} C_w^{r_4} \exp\left(-\frac{E_4 + PV_4}{RT}\right), \tag{5}$$

Here $\dot{\epsilon}_i$ (in s^{-1}) denotes the strain rate for each creep mechanism under dry or wet conditions, for example, $\dot{\epsilon}_1$ represents diffusion creep under dry conditions. It is a function of the average grain size, d (in microns), the deviatoric stress, σ (in MPa), the pressure, P (in Pa), and the absolute temperature, T (in K), and R is the gas constant. Strain rate also depends on the water content, C_w (in ppm H/Si), under wet conditions. The wet flow laws are expressed in terms of water content rather than water fugacity because we consider the mantle to behave as a closed system in the context of our modeling. The flow law parameters p_i, n_i, and r_i in Equations 2–5 are the grain size, stress, and water content exponents, respectively. The dependence of strain rate on temperature and pressure in all flow laws is characterized by the activation energy, E_i, and the activation volume, V_i, respectively. The scaling coefficient for the ith flow law, A_i, is in s^{-1} MPa^{-n_i} μm^{p_i} under dry conditions.

Using Equations 2–5 to evaluate strain rates due to diffusion and dislocation creep, our composite rheological model is expressed as

$$\dot{\epsilon}_{tot,j} = \dot{\epsilon}_{diff,\,j} + \dot{\epsilon}_{disl,j} \tag{6}$$

where $\dot{\epsilon}_{tot,j}$ denotes the total strain rate and the subscript j indicates either dry or wet conditions, and $\dot{\epsilon}_{diff,j}$ and $\dot{\epsilon}_{disl,j}$ denote the individual contributions of diffusion and dislocation creep, respectively. Note that only the dry flow laws are used to predict viscosity under dry conditions, and only the wet flow laws model wet rheology. We use the composite rheological model [Equation 6] with the flow law parameters reported by Jain et al. (2019) to estimate olivine rheology. In particular, the composite flow law for case OL-DB_2 in Jain et al. (2019) is used to model dry rheology and that for case OL-WB_1 to model wet rheology in our study.

2.2.2. Perturbation of Mean Flow Laws

Jain et al. (2019) constrained flow law parameters by analyzing multiple data sets on the deformation of olivine aggregates by using MCMC inversion. To conduct probabilistic geodynamic modeling, the mean value estimated for each parameter, denoted by $\langle q_k \rangle$ for the kth parameter, the associated standard deviation, $\sigma\left(q_k\right)$, and the correlation coefficient between different pairs of flow law parameters are used to construct a range of permissible flow laws. A set of M perturbed flow laws, containing K number of flow law parameters, is generated as follows. First, using the Cholesky decomposition of the correlation coefficient matrix, a matrix P of correlated, normally distributed random numbers of size $M \times K$ is constructed (e.g., Rubinstein, 1981, section 3.5.3). Next, a perturbed flow law parameter is generated using the following equation,

$$q_k^m = \langle q_k \rangle + \sigma\left(q_k\right) P_{mk}, \tag{7}$$

where m runs from 1 to M and k from 1 to K. Finally, in accordance with Jain et al. (2019), the perturbed values of A_i are normalized to 1,523 K and 0.3 GPa using the perturbed values of E_i and V_i.

Because dry and wet data were analyzed separately by Jain et al. (2019), they are assumed to be independent of each other and randomized separately, with $K = 6$ for the dry flow laws [Equations 2 and 4] and $K = 10$ for wet flow laws [Equations 3 and 5]. Note that the activation volumes under dry conditions have not been included in the count for K as they were not constrained by Jain et al. (2019). Instead, we selected M uniformly distributed random values within the range of 0–40 cm^3 mol^{-1} for each of the activation volumes V_1 and V_3. As for the wet flow laws, the uncertainties of the activation volumes V_2 and V_4 may have been

Table 1
Revised Estimates on the Flow Law Parameters for the Composite Rheological Model (6) for Olivine Aggregates Under Dry Conditions Yielded by Our Probabilistic Geodynamic Approach for the Cases $S2d_{10}$ and $S2d_{eq}$

Mechanism	Parameters	OL-DB$_2$ (Jain et al., 2019)	$S2d_{10}$ Our results	$S2d_{eq}$ Our results
Dry diffusion	p_1	2.11 ± 0.15	2.11 ± 0.13	2.10 ± 0.13
	E_1 (KJ mol^{-1})	370 ± 15	370 ± 19	369 ± 16
	V_1 (cm^3 mol^{-1})	0–40[a]	24 ± 7	19 ± 8
	A_1	$10^{7.86 \pm 0.15}$	$10^{8.10 \pm 0.18}$	$10^{8.00 \pm 0.16}$
Dry dislocation	n_3	3.64 ± 0.09	3.63 ± 0.08	3.65 ± 0.07
	E_3 (KJ mol^{-1})	424 ± 23	426 ± 13	423 ± 13
	V_3 (cm^3 mol^{-1})	0–40[a]	33 ± 5	29 ± 9
	A_3	$10^{2.10 \pm 0.20}$	$10^{2.46 \pm 0.19}$	$10^{2.34 \pm 0.18}$

Note. The two cases ($S2d_{10}$ and $S2d_{eq}$) differ in our assumption on the grain size distribution in the upper mantle. Our results are compared with the estimates that were obtained by analyzing experimental data on the deformation of olivine aggregates under dry conditions for the same rheological model using the MCMC inversion scheme (Jain et al., 2019) and were also used as input parameters to conduct probabilistic geodynamic modeling in the present study. Parameter p_1 is the grain size exponent for diffusion creep, n_3 the stress exponent for dislocation creep, E_1 and E_3 the respective activation energies for the two mechanisms in kJ mol^{-1}, V_1 and V_3 their activation volumes in cm^3 mol^{-1}, and A_1 and A_3 their respective scaling coefficients. The mean values of model parameters for diffusion and dislocation creep are reported, along with their 1 standard deviation. Correlation coefficients are reported in Tables S2 and S3 in the supporting information.
[a]Activation volumes were not constrained in Jain et al. (2019). We assumed these parameters to vary uniformly between 0–40 cm^3 mol^{-1}.

underestimated because the errors of high-pressure data could be larger than reported (Jain et al., 2019). We therefore used 2σ uncertainty for V_2 and V_4.

The mean values of flow law parameters and their uncertainties used in our study are listed in Tables 1 (OL-DB$_2$) and 2 (OL-WB$_1$), and the correlation coefficients are provided in Tables S5 and S15 of Jain et al. (2019). An ensemble of randomized flow laws for olivine are used to predict upper mantle viscosity in our geodynamic model described next.

2.3. Our Ridge Flow Model

Our two-dimensional model for the upper mantle spans the top 400 km of the Earth and from the ridge axis on the left to a distance of 6,000 km to its right. The domain is discretized into 301×61 elements with heterogeneous spacing. We model steady-state corner flow here by solving the Stokes flow equation for an incompressible, infinite Prandtl number fluid using the finite element code of Korenaga and Jordan (2003). Table S1 provides a list of parameters used in our geodynamic model.

The flow is assumed to be driven only by surface plate motion. To model ridge flow beneath the Pacific plate, a surface velocity of 7 cm yr^{-1} is prescribed. The stress-free boundary condition is assumed at the base but the velocity boundary conditions on the left and the right boundaries vary with our assumption on shear flow. For the reference case, denoted as case $S0$, zero flow is permitted normal to the left boundary, that is, free-slip boundary condition, and the right boundary is stress free. Consequently, the resultant steady-state horizontal velocity profile at the right boundary, denoted by $U_{S0}(x = right, z)$, represents the net horizontal shearing in the model domain for the case $S0$. Here, the steady-state horizontal and vertical velocity solutions are represented as $U_{S0}(x, z)$ and $V_{S0}(x, z)$, respectively.

In this study, we also explore the possibility of additional background shearing in the upper mantle and test some plausible synthetic horizontal shear flow profiles $S1$–$S5$. For the total horizontal flow to assume a shape $S_j(z)$, an additional horizontal flow of $\Delta S_j(z) = S_j(z) - U_{S0}(x = right, z)$ must be introduced in the model domain. This is achieved by imposing the synthetic horizontal flow profile S_j at the right boundary and the additional horizontal shear flow $\Delta S_j(z)$ at the left. The sum of the velocities $U_{S0}(x, z = bottom)$ and $\Delta S_j(z = bottom)$ is assigned to the bottom boundary and a surface velocity of 7 cm yr^{-1} is retained. To prevent the additional horizontal flow introduced at the left boundary from flowing out through the bottom of the domain, the vertical velocities at all boundaries are fixed at the steady-state solution for case $S0$, that is, $V_{S0}(x = left, z)$, $V_{S0}(x, z = top)$, $V_{S0}(x = right, z)$, and $V_{S0}(x, z = bottom)$ at the left, top, right, and bottom boundaries, respectively.

Table 2
Revised Estimates on the Flow Law Parameters for the Composite Rheological Model (6) for Olivine Aggregates Under Wet Conditions Yielded by Our Probabilistic Geodynamic Approach for the Cases $S2d_{10}$ and $S2d_{eq}$

Mechanism	Parameters	OL-WB$_1$ (Jain et al., 2019)	$S2d_{10}$ Our results	$S2d_{eq}$ Our results
Wet diffusion	p_2	1.74 ± 0.12	1.85 ± 0.15	1.69 ± 0.14
	r_2	0.84 ± 0.26	0.69 ± 0.20	0.94 ± 0.21
	E_2	362 ± 60	355 ± 54	365 ± 58
	V_2	6.75 ± 26.46[a]	20.99 ± 4.22	16.64 ± 4.49
	A_2	$10^{5.56 \pm 0.47}$	$10^{5.60 \pm 0.58}$	$10^{5.72 \pm 0.54}$
Wet dislocation	n_4	4.45 ± 0.32	4.28 ± 0.24	4.41 ± 0.19
	r_4	2.00 ± 0.02	2.00 ± 0.01	2.00 ± 0.01
	E_4	425 ± 190	464 ± 155	427 ± 154
	V_4	27.96 ± 16.24[a]	28.35 ± 6.59	27.20 ± 6.73
	A_4	$10^{-4.47 \pm 0.83}$	$10^{-2.88 \pm 0.88}$	$10^{-4.55 \pm 0.82}$

Note. The two cases ($S2d_{10}$ and $S2d_{eq}$) differ in our assumption on the grain size distribution in the upper mantle. Our results are compared with the estimates that were obtained by analyzing experimental data on the deformation of olivine aggregates under wet conditions for the same rheological model using the MCMC inversion scheme (Jain et al., 2019) and were also used as input parameters to conduct probabilistic geodynamic modeling in the present study. Parameter p_2 is the grain size exponent for diffusion creep, n_4 the stress exponent for dislocation creep, r_2 and r_4 the respective water content exponents for the two mechanisms, E_2 and E_4 their activation energies in kJ mol^{-1}, V_2 and V_4 their activation volumes in cm^3 mol^{-1}, and A_2 and A_4 their scaling coefficients. The mean values of model parameters for diffusion and dislocation creep are reported, along with their 1 standard deviation. Correlation coefficients are reported in Tables S2 and S3.
[a]The error in V_2 and V_4 for model OL-WB$_2$ listed here is double the value reported in Jain et al. (2019). This is because the high-pressure experimental data used in their study are expected to have larger than reported error; consequently the uncertainty in these parameters reported by Jain et al. (2019) may have been an underestimation.

For the prescribed surface velocity, the width of our domain encompasses seafloor ages from 0 at the ridge to ~85 Myr at x = 6,000 km (Figure S1). The temperature field is assumed to follow the half-space cooling model. Surface is assumed to be at 273 K, and the temperature at the base is fixed at the potential temperature of 1,623 K. When evaluating mantle rheology, potential temperature is converted to actual temperature using an adiabatic gradient of 0.5 K km^{-1}.

The composite flow law [Equation 6] for olivine aggregates is used to model upper mantle viscosity. Dry rheology is assumed in the lithosphere whereas wet flow laws model viscosity of the asthenosphere. The water content of the asthenosphere governs the depth of the dry to wet transition (Hirth & Kohlstedt, 1996). Additionally, a grain size distribution must be assumed to model deformation due to diffusion creep (Equations 2 and 3). It is common for geodynamic studies to assume a constant grain size of 1–10 mm throughout the upper mantle (e.g., Hedjazian et al., 2017; Kneller et al., 2005; Spiegelman & McKenzie, 1987; Stadler et al., 2010). Grain sizes are, however, more likely to vary across the upper mantle, and the influence of this assumption on our model predictions can be tested by comparing simulations for a constant grain size of 10 mm with those for a variable grain size distribution (section 3.1).

Grain size distribution in the upper mantle is not well constrained. High temperatures facilitate grain growth in the diffusion creep regime (e.g., Karato, 1989) whereas processes such as dynamic recrystallization in the dislocation creep regime can reduce grain size. The kinetics of both processes are not well understood, and a number of piezometer equations have been suggested to model the equilibrium grain sizes (e.g. "Table 13.2 of Karato, 2008). For the variable grain size case, therefore, we use the piezometer equation by Van der Wal et al. (1993) to predict grain size distribution in our model domain. This equation models dynamically recrystallized grain size, denoted by d_p, as the following nonlinear function of stress:

$$d_p = 10^{4.14}\sigma^{-1.33}, \tag{8}$$

where stress, denoted by σ, is in MPa and d_p in microns. Furthermore, we assume rapid grain growth in the diffusion creep regime. Under this condition, if dynamic recrystallization drives a grain into the diffusion creep regime, rapid grain growth will bring the grain size to the boundary between diffusion and dislocation

creep. This value of grain size at the mechanism boundary, represented by d_b, is evaluated by equating the strain rates for both mechanisms; for example, equating Equations 2 and 4 gives

$$d_b = \frac{A_1}{A_3}\sigma^{1-n_3}\exp\left(\frac{\left[E_1 - E_3\right] + P\left[V_1 - V_3\right]}{RT}\right). \tag{9}$$

The steady-state grain size at each point in our model domain, represented by d_{eq}, is, therefore, evaluated as,

$$d_{eq} = \max\left(d_p, d_b\right). \tag{10}$$

Additionally, the largest grain size is set to 10 cm, to avoid unrealistically large grains.

Our formulation for calculating "equilibrium" grain sizes is not unique; studies such as De Bresser et al. (2001) and Behn et al. (2009) have discussed other possible models. Behn et al. (2009), in particular, accounted for the time required for the grain size to reach steady state under a simple plate-shear flow and studies the impact of grain size evolution on the seismic structure below an oceanic plate. Considering the range of possible grain size evolution models and uncertainties in the parameters therein (e.g., Behn et al., 2009; Chu & Korenaga, 2012), our formulation, with the assumption of instantaneous grain growth, may serve as an end-member case.

With these assumptions on the water content and grain size distribution, our geodynamic model is run with an ensemble of at least 1,500 perturbed flow laws, where each realization of the perturbed flow law is consistent with experimental data. Different sets of perturbed flow law parameters generate unique simulations of ridge flow with distinct viscosity and strain rate fields (see, e.g., Figure S1a). We also compute hypothetical strain rates according to the dry flow law in the wet regions of the model. If strain rates predicted by the dry flow law are larger than those predicted by the wet flow law, then that combination of dry and wet composite flow laws is outright rejected, because deformation experiments indicate weakening of olivine samples in the presence of water (e.g., Hirth & Kohlstedt, 1996; Karato & Jung, 2003).

With the remaining flow laws, we proceed to evaluate the individual contributions of diffusion and dislocation creep to the total strain rate (Figure S1b), which will also differ among different realizations of the perturbed flow laws. Resultant velocity-gradient and strain rate fields, together with the strength of dislocation creep relative to the total strain rate, serve as input parameters to the D-Rex code.

2.4. Modeling Radial Anisotropy

We use the D-Rex code (Kaminski et al., 2004) to model the development of lattice-preferred orientation in the upper mantle. The code computes the average elastic tensor for an assemblage of grains at each point along the streamline. The radial anisotropy parameter, denoted by ξ, may be inferred from the elastic tensor, C, as $\xi = N/L$, where

$$N = \frac{1}{8}\left(C_{11} + C_{22}\right) - \frac{1}{4}C_{12} + \frac{1}{2}C_{66} \tag{11}$$

and

$$L = \frac{1}{2}\left(C_{44} + C_{55}\right) \tag{12}$$

The formulation for the code has been provided by Kaminski et al. (2004), and its predictions have been tested against experimental observations. We consider an aggregate of 2,200 grains with 70% olivine and 30% enstatite to evaluate radial anisotropy in our model using the D-Rex code. The assumed composition is a first-order approximation of the pyrolite model and moderates the otherwise strong anisotropy that is predicted with only olivine (Kaminski et al., 2004).

The A-type fabric is likely to develop in the dry regions, and the E-type fabric in hydrated regions of the upper mantle (e.g., Karato et al., 2008). The resolved shear stress for the different slip systems in olivine and enstatite and for each fabric type are obtained from Kaminski et al. (2004) and Becker et al. (2008). The effects of temperature and pressure on the elastic tensor (up to linear derivatives) for olivine and enstatite are also included. Reference values and pressure derivatives for olivine are from Abramson et al. (1997) and temperature derivatives from Isaak (1992). Reference values and pressure derivatives for enstatite are from Chai et al. (1997).

The D-Rex code is based on some assumptions that may impact our estimates on radial anisotropy in the upper mantle. The first assumption is that lattice-preferred orientation develops only in the dislocation creep regime. To accommodate this, before we evaluate preferred orientation, we multiply the nonrotational component of the strain rate tensor by the relative strength of dislocation creep, that is, $\dot{\epsilon}_{disl,j}/\dot{\epsilon}_{tot,j}$, where the symbols have the same meaning as in Equation 6. However, deformation by diffusion creep might weaken existing fabric (e.g., Edington et al., 1976; Karato et al., 1995); therefore, the aforementioned assumption may not be robust. As the rate of possible weakening is not well quantified experimentally, however, testing a range of possibility is overly time-consuming, so we also assume the preservation of fabric in the diffusion creep regime. This is the same approach used in previous studies, thereby facilitating to identify differences introduced by our probabilistic approach.

The original D-Rex code also assumes a value of 3 for the stress exponent for dislocation creep for all slip systems. In contrast, single crystal data suggest differences in the stress dependence of different slip systems (Mullet et al., 2015). Moreover, our MCMC inversion scheme constrains the stress exponents n_3 and n_4 for dislocation creep in olivine aggregates under dry and wet conditions, respectively, at ∼4. In our study, therefore, instead of 3, we use the perturbed values of n_3 and n_4, which were used to run the geodynamic simulation, for the D-Rex code as well. More detailed understanding of the relationship between microscopic and macroscopic deformation processes is required to assess the validity of using aggregate flow law parameters to model anisotropy due to a particular slip system.

The code further requires to specify the following three parameters: (1) dimensionless grain boundary mobility, M^*, (2) dimensionless nucleation rate, λ^*, and (3) threshold dimensionless volume fraction, χ, below which strain is accommodated by diffusion creep and grain-boundary sliding and not by dislocation creep. Experimentally constrained values suggested by Kaminski et al. (2004) are as follows: $M^* = 125 \pm 75$, $\lambda \sim 5$, and $\chi = 0.3 \pm 0.1$. We use $\chi = 0.2$ and the mean estimates on the remaining parameters. The influence of reported uncertainty in M^* on our results can be easily tested under our probabilistic approach, but it is not likely to be significant, as indicated by the sensitivity tests performed by Kaminski et al. (2004). The aforementioned range of values of M^* is appropriate only under the assumption that grains entering the upper mantle from the transition zone are initially randomly oriented, which may be a reasonable expectation as phase change in the transition zone likely destroys existing fabric. However, a recent study suggested that much lower values of M^* on the order of 10 may be more appropriate for the upper mantle because initial conditions may not be isotropic near a mid-ocean ridge (Hedjazian et al., 2017). It is beyond the scope of our study to assess the theoretical validity of this assumption, and, therefore, we retain the assumption of $M^* = 125$ here.

Using the input parameters listed above along with the output of the ridge flow simulation (section 2.3), we use the D-Rex code to predict radial anisotropy beneath the seafloor ages of 17–23 Myr and 37–43 Myr. The horizontal average of the former set is assigned to a seafloor age of 20 Myr and that of the latter to a 40 Myr old ocean floor. Because seafloor ages are known with an error of ∼3 Myr (Müller et al., 2008), the horizontal averaging helps incorporate this uncertainty in our model predictions. For example, Figure S1c presents the average predictions on the radial anisotropy parameter, ξ, beneath the 20 and 40 Myr old seafloor corresponding to the ridge flow simulation shown in Figures S1a and S1b. Geodynamic models implemented with distinct flow laws would yield unique predictions of radial anisotropy. The misfit between our model predictions and tomographic data is evaluated to identify geophysically relevant flow laws and model assumptions.

2.5. Global Tomography Models on Radial Anisotropy

As mentioned earlier, global tomography models SAW642ANb (Panning et al., 2010), S362ANI (Moulik & Ekström, 2014), and SGLOBE-rani (Chang et al., 2015) are used to constrain flow law parameters in our study. Because of poor depth resolution in surface wave tomography data, especially at shallow depths, we consider data at depth intervals of ∼25 km below the Pacific plate. These tomography models provide estimates on the radial anisotropy parameter ξ for a range of plate ages (e.g., Figure 2a). As done for model predictions (section 2.4), for each tomographic model, we consider the mean of all estimates between ages 17–23 Myr at a given depth as the value of the radial anisotropy parameter at 20 Myr and the average over 37–43 Myr as the value at 40 Myr at that depth. The corresponding standard deviation indicates the uncertainty in each tomographic model. Model uncertainty is not reported by most of these studies and thus is not included.

The resultant radial anisotropy profile suggested by these three studies (Figures 2b and 2c) indicates large discrepancies, especially at shallow depths. Models S362ANI and SGLOBE-rani also predict $\xi \leq 1$ in shallow upper mantle, which could indicate either isotropic conditions ($\xi = 1$) or $V_{SV} < V_{SH}$ in this region. This contradicts the anisotropy measured in natural ophiolites (Christensen, 1984). To include these unresolved differences among tomographic models, we compare our predictions of radial anisotropy with the median of the three tomographic models, which is represented by ξ_{obs} in Equation 1 (black solid line in Figures 2b and 2c). If $\langle \xi_l \rangle$ and $\langle \sigma_{\xi_l} \rangle$, respectively, represent the mean prediction on ξ and the associated standard deviation corresponding to the lth tomography model, where l runs from 1 to 3 here, then the values $\langle \xi_l \rangle - \langle \sigma_{\xi_l} \rangle$ and $\langle \xi_l \rangle + \langle \sigma_{\xi_l} \rangle$ define the 68% confidence bounds about the mean prediction. By combining the intervals for the three studies, we can compute the maximum variation in the value of ξ_{obs} permitted by the three tomography models. Uncertainty in ξ_{obs} is defined as half of this maximum variation.

By implementing the probabilistic modeling scheme described above, we aim to reduce existing uncertainty associated with the flow laws for olivine rheology. The application of this model, however, also requires us to make some assumptions on parameters such as the grain size distribution and shear flow in the upper mantle, which can also affect our predictions of radial anisotropy. Our probabilistic approach allows us to assess the relevance of these model parameters and arrive at a more realistic geodynamic model to explain the tomographic estimates on radial anisotropy. In the next section, we test our model predictions for a number of geodynamic scenarios based on our assumptions on the asthenospheric water content, the grain size distribution, and the background shear flow beneath the Pacific plate.

3. Results

The water content in the asthenosphere is expected to range between ~300–810 ppm H/Si (Hirth & Kohlstedt, 1996). The grain size distribution in the upper mantle (Chu & Korenaga, 2012; Lallemant et al., 1980) and shear flow under the Pacific (French et al., 2013; Steinberger et al., 2004) are only loosely constrained, and the probabilistic modeling approach can be used to derive plausible estimates on these variables. To do so, we run our geodynamic model with a particular assumption on each of the aforementioned parameters and an ensemble of over 1,500 perturbed flow laws. For each set of assumptions, therefore, we simulate more than 1,500 distinct models of radial anisotropy and compare our predictions with tomography models at 20 and 40 Myr. We discuss models with sufficiently small misfits, that is, $\chi^2/N < 1.3$.

3.1. Constraining the Water Content and the Grain Size Distribution in the Upper Mantle

First, we investigate the influence of the asthenospheric water content, C_{wa}, on our model predictions by comparing our estimates on radial anisotropy for two different assumptions on C_{wa}, that is, $C_{wa} = 500$ ppm H/Si and $C_{wa} = 810$ ppm H/Si. The depth of the dry-wet transition is estimated based on the influence of water content on the depth at which melting is initiated in the upper mantle below a mid-ocean ridge (Hirth & Kohlstedt, 1996). It is 100 km for $C_{wa} = 500$ ppm H/Si and 115 km for $C_{wa} = 810$ ppm H/Si. The grain size is assumed to be 10 mm (case d_{10}) throughout the upper mantle and no background shear flow is considered. Predictions of radial anisotropy with the assumption of $C_{wa} = 810$ ppm H/Si yield smaller misfits to seismic data (Text S1). Therefore, our analysis indicates that the asthenosphere beneath the Pacific plate may have high water content, with at least 810 ppm H/Si below 115 km depth.

With C_{wa} fixed at 810 ppm H/Si, we next repeat the probabilistic modeling of radial anisotropy with the assumption of spatially varying grain sizes (case d_{eq}) instead of constant grain size (case d_{10}). The grain size distribution was calculated based on our formulation of the "equilibrium" grain size (d_{eq}, Equation 10) discussed in section 2.3. With no background shear flow, both assumptions on the grain size distribution, that is, constant (d_{10}) as well as variable grain sizes (d_{eq}), produce similar fits to tomography models (Text S2).

However, even with the high asthenospheric water content, neither assumption on the grain size distribution could reproduce the tomographic predictions for radial anisotropy, specifically at depths of 100–200 km (Figure S2). Tomography indicates strong radial anisotropy with ξ significantly greater than 1 at these depths, whereas our models estimate a sharp decrease in ξ at the top of the asthenosphere. Our choice of model to estimate "equilibrium" grain sizes does not significantly affect our predictions of radial anisotropy. A more detailed model for the evolution of grain sizes in the upper mantle, for example, the ones tested by

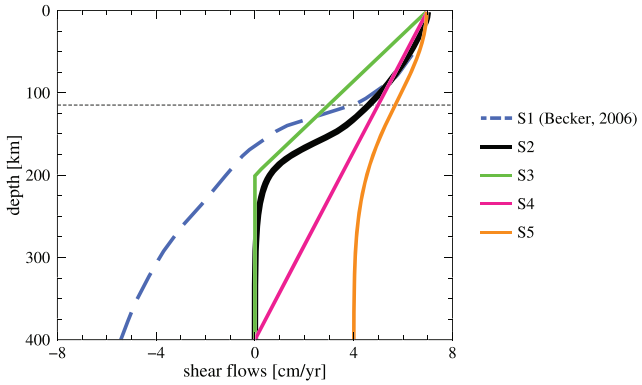

Figure 3. Five distinct shear flow profiles, labeled $S1$–$S5$, tested in our study. The synthetic flows $S2$–$S5$ were generated using the model predictions of Becker (2006) (profile $S1$, blue dashed line) as a reference.

Behn et al. (2009), might yield more reliable estimates on the grain size distribution. But, as indicated by their results, those estimates would lie in between our end-member cases (i.e., d_{10} and d_{eq}) and would, therefore, not improve the overall fit to anisotropy data.

To produce better agreement with seismic observations, therefore, our corner flow model must incorporate additional horizontal flow between 100 and 200 km depth, which could increase horizontal shear in this region and drive the a axis in olivine to realign subhorizontally, yielding $\xi > 1$. Such a background shear flow beneath the Pacific could be attributed to local sources, such as channel flows at the rheological boundary between the stiff lithosphere and weak asthenosphere, or to the net rotation of surface plates relative to the bulk of the mantle. Studies on subduction zone systematics (e.g., Uyeda & Kanamori, 1979) and global flow modeling (e.g., Becker, 2006; Conder et al., 2002; Conrad & Behn, 2010) have often suggested the existence of such flows. In the following section, we explore the geophysical feasibility of a range of background shear flow using our probabilistic modeling.

3.2. Investigating the Influence of Background Shear Flow on Our Model Predictions

Our results in the previous section suggest the need for additional shear flow beneath the Pacific plate, especially between 100 and 200 km depth, to produce strong radial anisotropy at that depth. We test five distinct shear flow profiles, labeled $S1$–$S5$ (Figure 3), to estimate the range of shear flows that may produce the optimum strain that is required to match tomographic estimates.

Synthetic flow profiles were constructed by introducing variations to a reference profile, $S1$ (Figure 3), which is suggested by the best fitting global flow model of Becker (2006). Profile $S1$ corresponds to his prediction for flow beneath the Pacific plate along a chosen cross section, which is perpendicular to the ridge axis and parallel to the direction of spreading. This profile comprises nonzero horizontal flow in the top ~200 km of the mantle in the same direction as the spreading velocity. Below that, the shear flow reverses direction and reaches velocities as high as 7 cm yr^{-1} at the base of the upper mantle. The remaining four test flow profiles were synthesized by varying the magnitude of flow of this reference profile as well as the sense of shearing. The surface plate velocity is fixed at 7 cm yr^{-1} for all cases.

Under our probabilistic modeling scheme, for each assumption on the shear flow profile, our geodyanamic model was implemented with an ensemble of over 4,000 perturbed realizations of the composite flow law. Successful models were characterized by $\chi^2/N < 1.3$, but to explicitly ensure good correspondence between the observations and the model predictions in the mid upper mantle region, we further eliminated those models that yielded average χ^2/N greater than 1.3 over the specific depth range of 100–200 km.

Using the updated criterion to assess modeling success, model fit is seen to improve most for one of our trial flow profiles, represented by $S2$ (Figure 3). Synthetic flow profile $S2$ is similar in shape to $S1$ but produces smaller peak velocities in the midmantle region. Cases $S2d_{eq}$ and $S2d_{10}$ correspond to two distinct assumptions on grain size distribution for the given shear flow. Irrespective of our assumption on the grain size distribution, some of our model predictions with this shear profile not only correspond to average $\chi^2/N < 1.3$ at 20 and 40 Myr but also produce close agreement with tomography over the particular depths of 100–200 km, with average χ^2/N lower than 1.2 over this depth range (Figure 4). Flow laws corresponding to the successful models here are next used to revise existing constraints on the flow law parameters for diffusion and dislocation creep in olivine. The new constraints imposed by cases $S2d_{10}$ and $S2d_{eq}$, which correspond to the assumption of constant and variable grain sizes, respectively, with background shear flow of $S2$, are summarized in Tables 1 and 2 and compared with the original MCMC-based estimates.

Both cases $S2d_{10}$ and $S2d_{eq}$ also appear to predict similar strain rate field beneath the Pacific plate, with a cold and strong lithosphere and a warmer and weaker asthenosphere (Figures 5a and 5d). The presence of water in the asthenosphere further weakens this region. Flow velocity (Figures 5a and 5d) is predicted to be mostly horizontal in the upper mantle except near the sides of our model domain. Surface spreading of the Pacific plate as well as the assumed shear flow profile create a "ridge pull" force near the ridge axis that induces mantle upwelling. Additionally, the imposed shear flow $S2$ forces flow at the base and the left

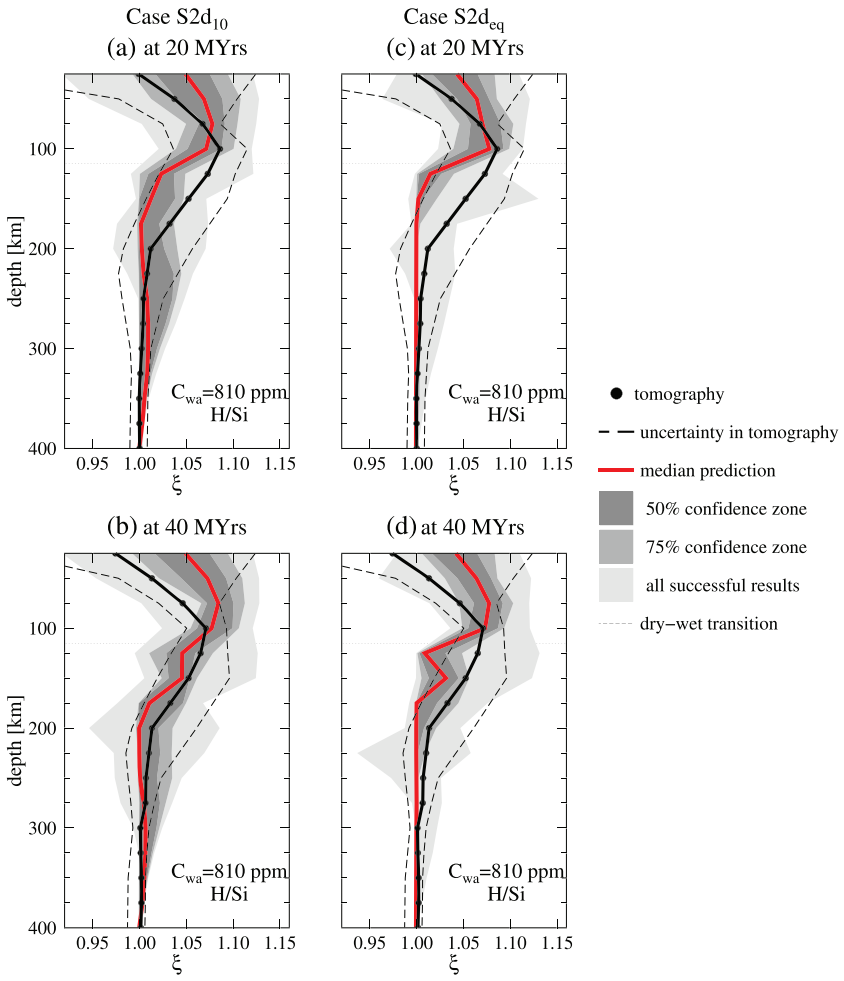

Figure 4. Comparison of the goodness of fit between the radial anisotropy profile suggested by tomography and that predicted by our geodynamic model when a background shear flow of *S*2 is assumed. Results of two different assumptions on the grain size distribution are compared. Panels on the left present radial anisotropy predictions at (a) 20 Myr and (b) 40 Myr corresponding to the assumption of a constant grain size of 10 mm throughout the upper mantle (case $S2d_{10}$). Panels on the right present results at (c) 20 Myr and (d) 40 Myr, respectively, for the assumption of a variable grain size distribution (case $S2d_{eq}$). A water content, C_{wa}, of 810 ppm H/Si is assumed below a depth of 115 km. Probabilistic modeling results of only the successful runs (normalized χ^2 over all data points and, in particular, between 100 – 200 km depth, is lower than 1.3) are shown here. Red line indicates the median prediction in each case, and shaded regions delineate the 50% (dark gray), 75% (lighter gray), and 100% (lightest gray) confidence zones. Our model predictions are compared with tomographic estimates on radial anisotropy (solid circles and solid line), which are also associated with some uncertainty (black dashed lines).

boundary of the asthenosphere to be in a direction opposite to the spreading plate, thereby creating some downwelling at the right boundary. For both these reasons, the stresses (not shown) are relatively higher near the side walls in our simulations. In contrast, flow is much slower in the bulk of the asthenosphere away from the ridge axis leading to lower stresses in this region. For the case $S2d_{eq}$, where grain size is a function of stress, this leads to relatively smaller grain sizes underneath ocean floor younger than 5 Myr or older than 75 Myr (e.g., Figure 5e) and grains as large as even 10 cm in size in the bulk of the upper mantle. The differences in grain size and stress distributions between cases $S2d_{10}$ and $S2d_{eq}$ affect the spacial extent of dislocation creep in the upper mantle (Figures 5b and 5f). For seafloor younger than 40 Myr, some successful models for case $S2d_{10}$ can predict stronger dislocation creep in the wet asthenosphere, which yields stronger anisotropy at these depths than the predictions for case $S2d_{eq}$ (e.g., Figures 5c and 5g). Both cases, however, fit tomographic estimates within acceptable error.

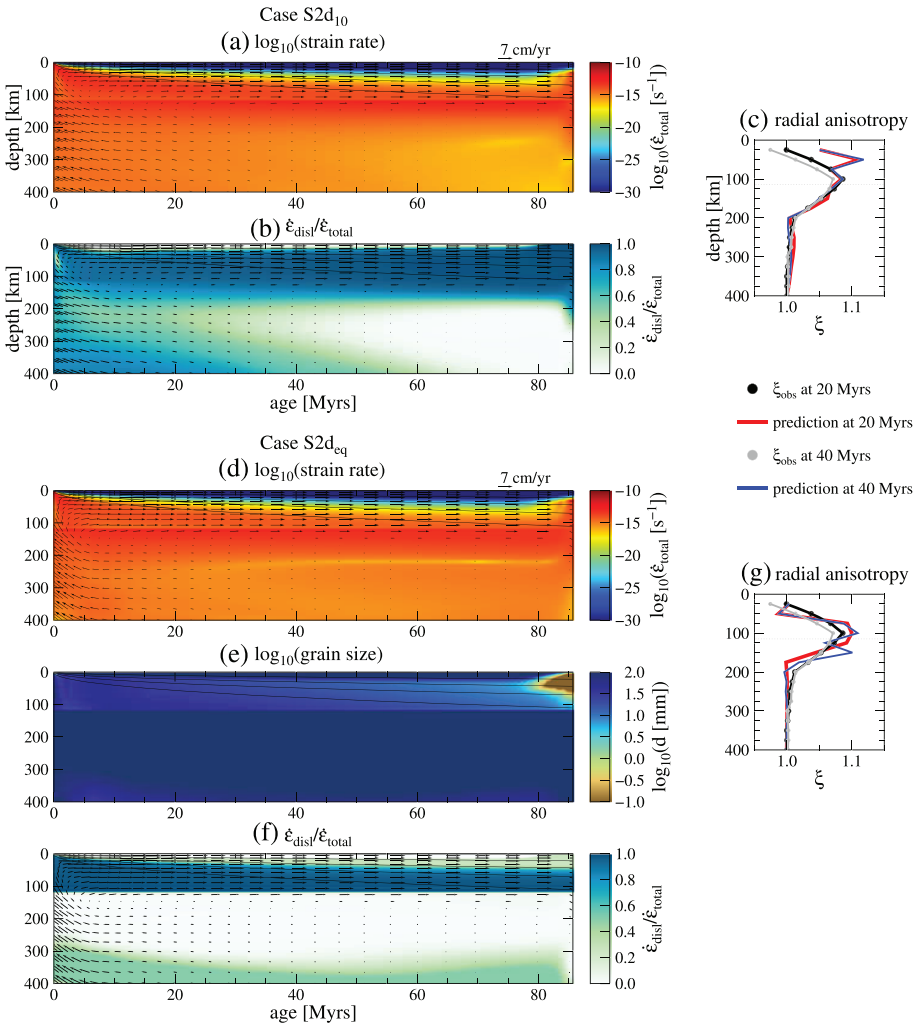

Figure 5. Sample output of ridge flow simulations with background shear flow $S2$ and two different assumptions on grain sizes. Case $S2d_{10}$ assumes a constant grain size of 10 mm throughout the upper mantle, whereas case $S2d_{eq}$ corresponds to a variable grain size distribution. The steady-state distributions of (a and d) total (composite) strain rate, $\dot{\epsilon}_{total}$, in the logarithmic space, and (b and f) fractional contribution of dislocation creep to the total strain rate, calculated as $\dot{\epsilon}_{disl}/\dot{\epsilon}_{total}$, are compared for the two cases, respectively. Here $\dot{\epsilon}_{disl}$ denotes strain rate owing to dislocation creep. The steady-state distribution of (e) grain size, d, in the logarithmic space, for the case $S2d_{eq}$ is also shown. Arrows in (a), (b), (d), and (f) indicate the direction of flow, and their length corresponds to the magnitude of flow velocity relative to the surface velocity of 7 cm yr^{-1}. (c and g) Predictions of radial anisotropy at 20 Myr (red) and 40 Myr (blue) for each flow simulation, respectively, compared with tomography data. These results correspond to the set of flow law parameters that produce smallest misfit to tomography data in each case. Asthenospheric water content is 810 ppm H/Si in both simulations.

3.3. New Constraints on the Flow Law Parameters for Olivine

Out of over 10,000 perturbed flow laws for olivine tested by us, only ~70 flow laws yielded acceptable predictions of radial anisotropy for the cases $S2d_{10}$ and $S2d_{eq}$. This subset of flow laws in each case is, therefore, consistent with experimental data and produces realistic predictions of radial anisotropy under the Pacific oceanic plate. We use these successful flow laws to revise existing constraints on the flow law parameters of olivine rheology. Tables 1 and 2 summarize the revised flow law parameters so obtained in the form of the mean and the standard deviation of each parameter. Tables S2 and S3 provide the correlations exhibited by the successful flow laws.

We find that the results of probabilistic modeling do not significantly modify the MCMC-derived constraints on most of flow law parameters, such as the stress exponent for dislocation creep or the activation energies for both diffusion and dislocation creep. The merit of our probabilistic modeling approach lies in its

constraints on the effect of pressure on olivine rheology. Cases $S2d_{10}$ and $S2d_{eq}$ yield an activation volume of 24 ± 7 and 19 ± 8 cm^3 mol^{-1}, respectively, for diffusion creep under dry conditions, denoted by V_1. For dislocation creep, probabilistic modeling yields values of 33 ± 5 (case $S2d_{10}$) and 29 ± 9 cm^3 mol^{-1} (case $S2d_{eq}$) for the activation volume under dry conditions, designated as V_3. The a posteriori probability distributions of the successful models in our study (Figures S4 and S5) indicate that both V_1 and V_3 are only loosely constrained, but these parameters were previously not constrained by the MCMC inversion of deformation data for lack of sufficient high-pressure experimental data under dry conditions (Jain et al., 2019).

Our analysis also yields tighter bounds on the activation volumes for both diffusion and dislocation creep under wet conditions, denoted by V_2 and V_4, respectively. Moreover, successful geodynamic models in our study correspond to higher values of V_2, in particular, than that suggested by MCMC inversion (Table 2). Our mean estimates on V_1 and V_3 are also higher than those suggested by past experimental studies. Additionally, case $S2d_{10}$ consistently corresponds to larger activation volumes than case $S2d_{eq}$. The significance of these results is discussed in the next section.

4. Discussion

Thus far, our analysis indicates that tomographic estimates on radial anisotropy are best explained with the assumption of the shear profile $S2$. Our probabilistic modeling with cases $S2d_{10}$ and $S2d_{eq}$ yields new estimates on the composite flow law for olivine rheology, but as seen in Tables 1 and 2, the most meaningful update is about the activation volumes; the uncertainties of other flow law parameters remain mostly unaffected. This is an important aspect of our radial anisotropy modeling because the activation volume has been among the most challenging parameters to determine experimentally. At the same time, however, the values of activation volume preferred by our modeling are rather surprising, pointing to a need to consider carefully how a composite rheology actually works.

Both cases $S2d_{10}$ and $S2d_{eq}$ constrain V_1 at $\sim 20 \pm 8$ cm^3 mol^{-1} (dry diffusion) and V_3 at $\sim 30 \pm 8$ cm^3 mol^{-1} (dry dislocation), which are notably higher than existing experimental estimates on V_3 of 15 ± 5 cm^3 mol^{-1} (Karato & Jung, 2003). Such high values of V_1 and V_3 are needed in our model to ensure that the presence of water in the asthenosphere weakens this region, in accordance with studies on the effect of water on olivine rheology (Karato, 2008, chapter 10). In other words, with lower values for V_1 and V_3, dry flow laws would predict faster deformation than wet flow laws.

The cause of high activation volumes for dry flow laws is easily traced to the a priori range for the activation volume for wet dislocation V_4, which is set to 28 ± 16 cm^3 mol^{-1} (Jain et al., 2019). This range is high compared to earlier compilations (e.g., 10–20 by Karato & Wu, 1993 and 11 by; Hirth & Kohlstedt, 1996), but broad enough to partially overlap with them. Moreover, it is the range that the existing experimental data indicates. In the global inversion of published deformation data under wet conditions (Jain et al., 2019), eight different possibilities were considered in total, with four of them for the combination of diffusion and dislocation creep, and the rest with the addition of dislocation-accommodated grain boundary sliding, and such a high activation volume was essential to avoid negative activation volume for coexisting deformation mechanisms. With the condition that dry flow laws need to be less effective than wet flow laws in the asthenosphere, the activation volumes for dry flow laws have to be even higher. This is supported by the small but positive correlations between V_1 and V_2 as well as V_3 and V_4 (Tables S2c and S3c). It may be possible to remove this condition if dry flow laws would become irrelevant under wet conditions. The number of experimental data in accord with this possibility is rather small (Figure 11 of Jain et al., 2019). Without this condition, radial anisotropy modeling would become insensitive to the activation volumes of dry flow laws, as the depth range of lithosphere is limited.

Also, with the high activation volume for wet dislocation V_4, the activation volume for wet diffusion V_2 also has to become similarly higher; otherwise, radial anisotropy would hardly develop in the asthenosphere. Case $S2d_{10}$ yields higher mean estimates on V_2 than the case $S2d_{eq}$ because the prominent increase in ξ_{obs} between 100 and 200 km depth can be reproduced only if this region deforms predominantly by dislocation creep. Such a requirement is met in the case $S2d_{eq}$ by assuming larger grain sizes at these depths (Figures 5f and 6). In the case $S2d_{10}$, larger V_2 compensates for the restricted variability in grain size. For the same reason, the grain size exponent p_2 and the activation volume V_2 for diffusion creep under wet conditions are also found to be weakly negatively correlated (Tables S2b and S3b). Our analysis also produced new

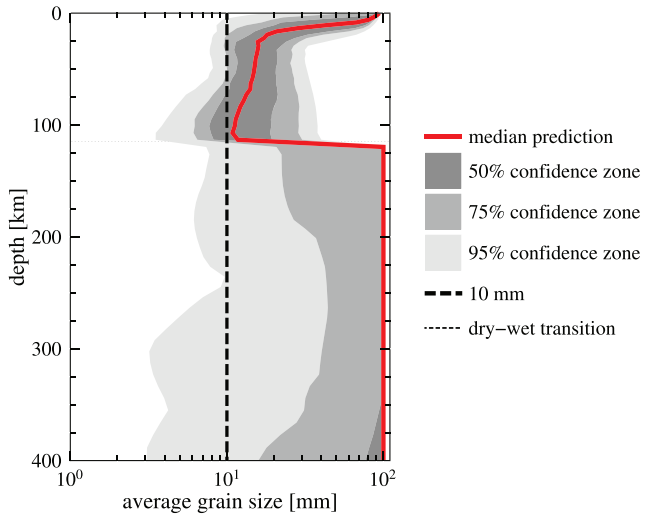

Figure 6. Variation of horizontally averaged grain size with depth, predicted by case $S2d_{eq}$, which corresponds to the assumption of variable grain size distribution and background shear flow of profile $S2$. The region below 115 km depth is considered wet, with a water content of 810 ppm H/Si. Results of only the successful models are shown. The median prediction is marked in red and is enclosed by the 50% (dark gray shaded region), 75% (lighter gray), and 95% (lightest gray) confidence zones. The assumption of a constant grain size of 10 mm (case $S2d_{10}$, black dashed line) is also shown for comparison.

correlations between some of the flow law parameters, such as the grain size and the water content exponents for diffusion creep under wet conditions.

These results warrant two additional remarks. First, our results are inherently biased by our assumption on the a priori bounds on all of the flow law parameters. This may appear problematic in light of the higher than expected values of the activation volumes yielded in our study, and we may be tempted to relax the assumed a priori bounds. Considering geophysical inversion as an independent means to constrain rheology may free it from the limitations associated with experimental data. However, we must reiterate that deformation experiments provide the most direct constraints on olivine rheology, and therefore, overlooking them completely would be imprudent. Because both experimental and geophysical data provide independent constraints on mantle rheology, and both data sets are associated with large uncertainties, it is best to use both simultaneously to design a self-consistent geodynamic model. Consequently, our probabilistic modeling approach provides a better way to extract the "useful" information contained in these data than that suggested by previous studies.

Second, the interpretation of our results can become limited by the scope of our model assumptions, and care should be taken to avoid this. For the particular case of the activation volumes, for example, the high values suggested by our successful models can also be interpreted as a general need for a large increase in mantle viscosity with depth. This requirement could be fulfilled in ways other than increasing the activation volume, for example, by anisotropic viscosity, compositional heterogeneity, different grain size model, or depth-dependent oxygen fugacity. Another merit of our probabilistic modeling approach lies in its ability to test the robustness of its results against different model assumptions. We demonstrate this below.

The shear profile $S2$ discussed in our study and, consequently, the revised constraints on the flow law parameters suggested here may not be unique in explaining tomography models. By testing a few possible shear flow profiles (Figure 3), we find that other assumptions on the background shear flow may also yield acceptably small misfits to observed seismic data. We next use our probabilistic geodynamic modeling approach to constrain plausible values of background shear flow beneath the Pacific plate.

4.1. Investigating Bounds on the Background Shear Flow and Strain

We explored the nonuniqueness in our assumption of the background shear flow by testing five different shear flow profiles, including profile $S2$. Similar to our analysis with $S2$ (section 3.2), for each of the remaining four assumptions too, approximately 1,000 perturbed flow laws were used to simulate radial anisotropy, and normalized χ^2 values were computed over all depth points as well as over the specific depth range of 100–200 km. The goodness of fit between the tomographic estimates on radial anisotropy and our predictions, corresponding to all assumptions on shear flow, is compared in Figure 7.

Profile $S1$ is the shear flow suggested by the global flow field predicted by Becker (2006). It indicates strong horizontal flow in the dry region of our model domain (Figure 3). The flow reverses direction below the dry-wet transition depth, causing large shearing in the midmantle region and strong flow at the base of the mantle, similar in magnitude but opposite in direction to the surface plate motion. Profiles $S3$ and $S5$ are designed similar to $S2$ but differ in the magnitude of shear introduced. Profile $S3$ also introduces horizontal shear flow only in the top half of the upper mantle but with velocity decreasing linearly from 7 cm yr^{-1} at the surface to zero at ~200 km depth, unlike profile $S2$, which has a velocity jump near this depth. Profile $S5$ also shows a smaller velocity jump at ~200 km depth; instead of the zero velocity below this depth as in $S2$, profile $S5$ introduces a constant horizontal velocity of 4 cm yr^{-1} in the lower half of the upper mantle. Profile $S4$ is the simplest form of shearing, with linearly decreasing velocity from the surface at 7 cm yr^{-1} to zero at the base.

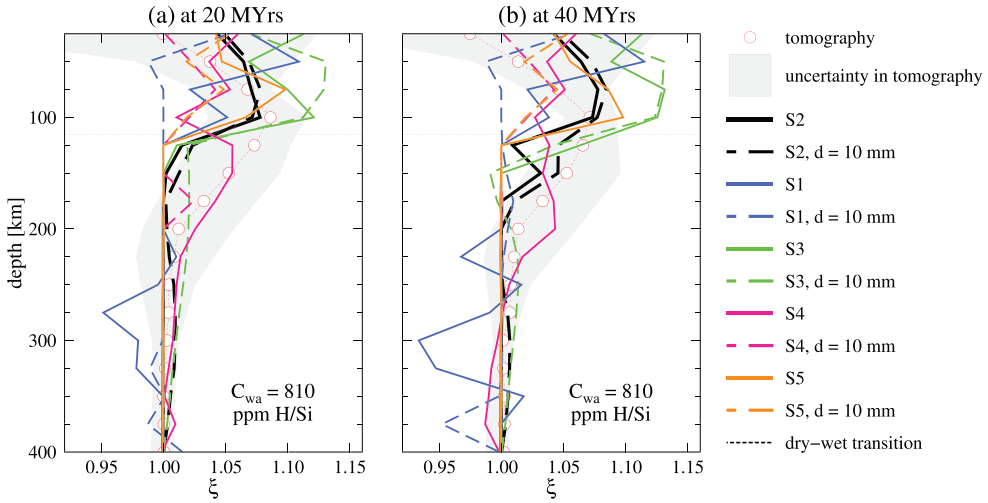

Figure 7. Comparison of the estimates on the radial anisotropy parameter, ξ, produced by five different assumptions, that is, *S*1–*S*5 on the background shear flow in our geodynamic model. The median prediction of all successful models is shown for flow profile *S*2, whereas for flow profiles *S*1 and *S*3–*S*5, the predictions that yield the lowest misfit to tomography results are shown. The radial anisotropy profile is estimated at two lithospheric ages, (a) 20 Myr and (b) 40 Myr. Different colors represent distinct assumptions on flow. Solid lines denote results corresponding to the assumption of variable grain sizes whereas dashed lines indicate the assumption of constant grain size. Asthenospheric water content C_{wa} of 810 ppm H/Si is assumed below 115 km depth in all cases. The tomographic estimates on radial anisotropy (red circles and red dotted line) at both lithospheric ages, with the associated uncertainty (gray-shaded area) are also shown for comparison.

Probabilistic modeling with these velocity boundary conditions yielded largest misfits for the *S*1 profile for both the variable grain size (case d_{eq}) as well as the constant grain size assumption (case d_{10}). In particular, this case produced weaker than expected anisotropy below 100 km. Because of the strong shear flow imposed by this profile at the base, streamlines for the same case tend to accumulate more dislocation strain below 200 km (Figure 8). However, the reversal in the direction of flow induced by this profile at ~150 km depth (Figure 3) can cause streamlines to curve and loop below this depth. Therefore, despite possibly large strains, the direction of flow may be subvertical, yielding $\xi \leq 1$ here. Not much strain is added between 120 and 200 km depth as diffusion creep tends to dominate, and perhaps this is why the predictions for anisotropy are ~1 at these depths (Figure 7) whereas tomography indicates stronger anisotropy between 120 and 200 km (Figure 2). The anisotropy prediction for this case shown in Figure 7 corresponds to one particular model with the smallest χ^2/N. All models produced $\chi^2/N > 1.4$ in this case and were, therefore, rejected.

The velocity boundary conditions *S*3–*S*5 yielded radial anisotropy predictions that fit tomography models more closely (average $\chi^2/N < 1.3$) at 20 as well as 40 Myr. The constant grain size assumption for these cases, however, produces lower than expected anisotropy (Figure 7) and thereby larger misfit in the 100–200 km depth range. It is likely that larger dislocation strain or stronger horizontal shear is needed in this depth range. The strain distribution can change if grain sizes are allowed to vary (Figure 8), and this assumption improves the fit for the cases $S3d_{eq}$ and $S4d_{eq}$. Our assumption on grain size distribution, however, has little influence on the total dislocation strain profile and the radial anisotropy predictions for the case *S*5, indicating the possibility that the horizontal shearing may be insufficient for this flow profile, preventing the formation of a stronger fabric. Additionally, the overall better performance of the cases *S*2–*S*5 with respect to *S*1 lowers the likelihood of such strong shear flows such as *S*1 beneath the Pacific plate.

In summary, synthetic shear flow profiles *S*2 and *S*4 tested in our study may indicate the minimum and maximum shear flows, respectively, which are required to produce optimum strain to match tomographic estimates on radial anisotropy. It is difficult to define the optimum value of total strain that could reproduce tomography results because not only the magnitude of strain but also its spatial distribution and the direction of shearing affect the evolution of lattice-preferred orientation. Reducing uncertainty in tomographic estimates may help determine tighter constraints on shear flow as well as strain. Since our assumption on shear flow could influence our constraints on the flow law parameters for olivine rheology, nonuniqueness in our estimates on both may be reduced if one or more of the following become available: independent

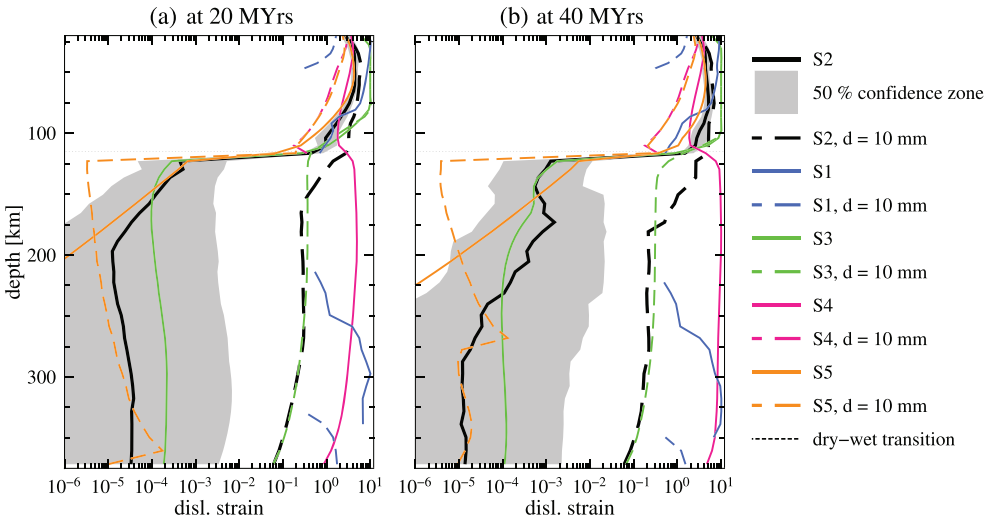

Figure 8. Total strain undergone by grains as they flow along a stream line to reach different depths below the lithospheric plate of ages (a) 20 Myr and (b) 40 Myr, respectively. Different colors correspond to results for the five different assumptions on background shear flow, represented by profiles *S*1–*S*5. Median predictions for all successful models are shown for shear profile *S*2, whereas for flow profiles *S*1 and *S*3–*S*5, strain predictions of only the models that yield the lowest misfit to tomography results are shown. Apparent gap in the strain profiles in the midmantle region for a few cases indicates zero strain, which could not be plotted on a logarithmic scale. Solid and dashed lines indicate the assumptions of variable and constant grain size, respectively. The 50% confidence zone about the median prediction for case $S2d_{eq}$ is also provided (gray-shaded region); larger uncertainties are associated with the predictions of other shear profiles. Water content of 810 ppm H/Si is assumed below 115 km depth in all cases.

geophysical constraints on mantle flows and grain sizes, more high-quality experimental data spanning a wide range of conditions, and tomography models with better depth resolution. Note that our estimates may be improved if data from oceanic floors older than 40 Ma are also included. In this study, however, we chose to restrict our predictions on radial anisotropy underneath relatively young oceanic floor, that is, within 60 Ma, because mantle flow may not be stationary under older ocean floor (e.g., Becker, 2006). Even at 40 Ma, the streamlines can sometimes become quite complicated in the midmantle region, and the D-Rex code might not be designed to handle such flow geometries.

The East Pacific Rise marks a divergent boundary between the Pacific and the Nazca plates, with the Pacific plate moving westward and the Nazca plate eastward. Similar to our analysis for the Pacific plate, it is possible to simulate ridge flow beneath the Nazca plate and model radial anisotropy therein. The results of probabilistic modeling for the Nazca plate could help constrain the spatial extent of the shear flow suggested by our analysis of the Pacific plate. If successful models for the Nazca plate favor a different shear flow profile from the Pacific plate, then the background shear flow constrained in our study is likely to be more regional, that is, exist only beneath the Pacific plate; otherwise, it may be more global. In general, investigating other oceanic plates as well as incorporating more observational constraints such as azimuthal anisotropy should shed more light on the reliability of our results, and probabilistic geodynamic modeling provides a natural framework to explore such possibilities.

5. Summary and Outlook

In summary, we introduced a new probabilistic approach to utilize geophysical observations to improve our understanding of rock mechanics via geodynamic modeling, and, as a representative example, we implemented it using radial anisotropy beneath the Pacific plate. The probabilistic modeling approach helped identify a range of flow law parameters that are consistent with experimental deformation data as well as tomographic models for radial anisotropy. It also indicated the plausibility of a wet and strongly sheared asthenosphere beneath the Pacific plate. Probabilistic geodynamic modeling, therefore, presents a major step forward to combine the fields of experimental rock mechanics and observational geophysics to facilitate multidisciplinary research on mantle dynamics. Although the role of experimental studies is indispensable

in understanding rock rheology, experiments can only explore a limited range of conditions, and uncertainties increase when extrapolated to realistic mantle conditions. Our new approach provides a powerful complement to improve existing constraints on mantle rheology. Its application can also supplement the information on local or global mantle dynamics that is gleaned from observational geophysical techniques.

In this work, the validation of our model assumptions is necessarily limited because this is a first step to demonstrate the benefit of probabilistic modeling, and as such, a range of possibilities, such as the effect of diffusion creep on fabric strength and the initial anisotropy of the incoming mantle, remain unexplored. Some input parameters for the D-Rex code are not experimentally well constrained (section 2.4), and our analysis could greatly benefit from investigating the influence of such parameters as well. Our assumption on the grain size distribution in the upper mantle is another aspect worth inspecting further. Our current formulation is rather simplistic and often produces too large grain sizes. Grain growth kinetics are expected to be more complicated in the mantle because of the influence of variable temperature and water content as well as the presence of other minerals. The effect of such factors can be tested under the probabilistic geodynamic modeling scheme. In our study, we have adopted the most straightforward method of conducting probabilistic modeling, that is, we extensively sample the flow law space to run a range of forward models and construct the a posteriori probability distribution of the flow law parameters based on the model results. Depending on the geodynamic model, more sophisticated optimization techniques may be adopted to search for the "best fit" set of parameters without exhaustively sampling the entire parameter space. However, the point of our probabilistic modeling approach is to illustrate the correct way to construct the parameter space to be sampled such that the outcome is consistent to experimental as well as geophysical data. This aspect has been overlooked in previous studies on geophysical inversion.

The greatest advantage of our approach is its potential to accommodate a number of constraints and explore a range of model assumptions to quantify their geophysical relevance. This not only allows the identification of the most plausible set of assumptions but also helps assess the scope for improvement even in the best fitting model. Any model is only as reliable as its least robust assumption, and the identification of weak assumptions could open new avenues for research. For example, based on our results, seismic studies may be conducted in future to verify the existence of strong shear flow beneath the Pacific plate and characterize this shear flow, if present. These flows could have geodynamical implications, for example, they may influence the angle of plate subduction and trench retreat (e.g., Billen & Hirth, 2007; Doglioni et al., 1999; Ficini et al., 2017).

Our modeling results indicate that the radial anisotropy of the upper mantle is highly sensitive to the pressure dependence of olivine rheology, but at the same time, higher than expected values of the activation volumes suggested in this study point to the need for designing more accurate high-pressure deformation experiments. At the moment, it is difficult to refute such high activation volumes, without questioning the quality of the original experimental data that were used to derive the a priori range of flow law parameters or the basic tenet of composite rheology, and both issues deserve careful further studies. Until recently, it has been rare to analyze experimental data with a proper treatment of composite rheology, and the difficulty of resolving relevant flow law parameters unambiguously is yet to be appreciated widely. The situation is further compounded by the possibility that different slip systems depend differently on stress, water content, and pressure (Masuti et al., 2019; Mullet et al., 2015). The presence of melt, which has not been considered in our model, could also play an important role near the ridge as it could change the dominant slip system from A to possibly B (Hansen et al., 2016).

However, these important sources of uncertainty do not overshadow the prospects of probabilistic geodynamic modeling; rather, they only underline the merit of this new approach. When different deformation mechanisms coexist, and each mechanism depends on various thermodynamic parameters, the geological significance of individual flow law parameters can be understood only through their application to a proper large-scale context. Probabilistic geodynamic modeling, in conjunction with a thorough statistical analysis of deformation data, allows us to test the state-of-the-art understanding of experimental rock mechanics in a global setting, and its outcome will inevitably stimulate more rigorous collaborations among rock mechanics, mantle dynamics, and observational geophysics.

Data Availability Statement

Data for all tomography models used in this study are available through the Incorporated Research Institutions for Seismology (IRIS) website: "SAW642ANb" [https://doi.org/10.17611/DP/9991698],

"S362ANI" [https://doi.org/10.17611/DP/9991736], and "SGLOBE-rani" [https://doi.org/10.17611/dp/emc2015sgloberani]. Estimates on lithospheric age are available through Müller et al. (2008).

Acknowledgments
We would like to thank Shun-ichiro Karato for his invaluable guidance on the physics of the development of lattice-preferred orientation in olivine, which helped us implement the D-Rex code and interpret its results, keeping possible limitations in mind. Reviews from two anonymous reviewers were also helpful in improving this manuscript. This work was sponsored by the U.S. National Science Foundation under grant OCE-1417327. This work was also supported in part by the facilities and staff of the Yale University Faculty of Arts and Sciences High Performance Computing Center.

References

Abramson, E. H., Brown, J. M., Slutsky, L. J., & Zaug, J. (1997). The elastic constants of San Carlos olivine to 17 GPa. *Journal of Geophysical Research*, *102*(B6), 12,253–12,263.

Alisic, L., Gurnis, M., Stadler, G., Burstedde, C., & Ghattas, O. (2012). Multi-scale dynamics and rheology of mantle flow with plates. *Journal of Geophysical Research*, *117*, B10402. https://doi.org/10.1029/2012JB009234

Baumann, T. S., & Kaus, B. J. P. (2015). Geodynamic inversion to constrain the non-linear rheology of the lithosphere. *Geophysical Journal International*, *202*(2), 1289–1316.

Becker, T. W. (2006). On the effect of temperature and strain-rate dependent viscosity on global mantle flow, net rotation, and plate-driving forces. *Geophysical Journal International*, *167*(2), 943–957.

Becker, T. W., Kustowski, B., & Ekström, G. (2008). Radial seismic anisotropy as a constraint for upper mantle rheology. *Earth and Planetary Science Letters*, *267*(1–2), 213–227.

Behn, M. D., Hirth, G., & Elsenbeck II, J. R. (2009). Implications of grain size evolution on the seismic structure of the oceanic upper mantle. *Earth and Planetary Science Letters*, *282*(1–4), 178–189.

Billen, M. I., & Hirth, G. (2007). Rheologic controls on slab dynamics. *Geochemistry, Geophysics, Geosystems*, *8*, Q08012. https://doi.org/10.1029/2007GC001597

Chai, M., Brown, J. M., & Slutsky, L. J. (1997). The elastic constants of an aluminous orthopyroxene to 12.5 GPa. *Journal of Geophysical Research*, *102*(B7), 14,779–14,785.

Chang, S.-J., Ferreira, A. M. G., Ritsema, J., van Heijst, H. J., & Woodhouse, J. H. (2015). Joint inversion for global isotropic and radially anisotropic mantle structure including crustal thickness perturbations. *Journal of Geophysical Research: Solid Earth*, *120*, 4278–4300. https://doi.org/10.1002/2014JB011824

Christensen, N. I. (1984). The magnitude, symmetry and origin of upper mantle anisotropy based on fabric analyses of ultramafic tectonites. *Geophysical Journal International*, *76*(1), 89–111.

Chu, X., & Korenaga, J. (2012). Olivine rheology, shear stress, and grain growth in the lithospheric mantle: Geological constraints from the Kaapvaal craton. *Earth and Planetary Science Letters*, *333*, 52–62.

Conder, J. A., Forsyth, D. W., & Parmentier, E. M. (2002). Asthenospheric flow and asymmetry of the East Pacific Rise, MELT area. *Journal of Geophysical Research*, *107*(B12), 2344. https://doi.org/10.1029/2001JB000807

Conrad, C. P., & Behn, M. D. (2010). Constraints on lithosphere net rotation and asthenospheric viscosity from global mantle flow models and seismic anisotropy. *Geochemistry, Geophysics, Geosystems*, *11*, Q05W05. https://doi.org/10.1029/2009GC002970

De Bresser, J., Ter Heege, J., & Spiers, C. (2001). Grain size reduction by dynamic recrystallization: can it result in major rheological weakening?. *International Journal of Earth Sciences*, *90*(1), 28–45.

Doglioni, C., Harabaglia, P., Merlini, S., Mongelli, F., Peccerillo, A. T., & Piromallo, C. (1999). Orogens and slabs vs. their direction of subduction. *Earth-Science Reviews*, *45*(3–4), 167–208.

Edington, J. W., Melton, K. N., & Cutler, C. P. (1976). Superplasticity. *Progress in Materials Science*, *21*(1–2), 61–170.

Ficini, E., Dal Zilio, L., Doglioni, C., & Gerya, T. V. (2017). Horizontal mantle flow controls subduction dynamics. *Scientific Reports*, *7*(1), 1–7.

French, S., Lekic, V., & Romanowicz, B. (2013). Waveform tomography reveals channeled flow at the base of the oceanic asthenosphere. *Science*, *342*(6155), 227–230.

Hansen, L. N., Qi, C., & Warren, J. M. (2016). Olivine anisotropy suggests Gutenberg discontinuity is not the base of the lithosphere. *Proceedings of the National Academy of Sciences*, *113*(38), 10,503–10,506.

Hedjazian, N., Garel, F., Davies, D. R., & Kaminski, E. (2017). Age-independent seismic anisotropy under oceanic plates explained by strain history in the asthenosphere. *Earth and Planetary Science Letters*, *460*, 135–142.

Hirth, G., & Kohlstedt, D. L. (1996). Water in the oceanic upper mantle: implications for rheology, melt extraction and the evolution of the lithosphere. *Earth and Planetary Science Letters*, *144*(1–2), 93–108.

Isaak, D. G. (1992). High-temperature elasticity of iron-bearing olivines. *Journal of Geophysical Research*, *97*(B2), 1871–1885.

Jain, C., Korenaga, J., & Karato, S.-I. (2018). On the grain size sensitivity of olivine rheology. *Journal of Geophysical Research: Solid Earth*, *123*, 674–688. https://doi.org/10.1002/2017JB014847

Jain, C., Korenaga, J., & Karato, S.-I. (2019). Global analysis of experimental data on the rheology of olivine aggregates. *Journal of Geophysical Research: Solid Earth*, *124*, 310–334. https://doi.org/10.1029/2018JB016558

Kaminski, E., Ribe, N. M., & Browaeys, J. T. (2004). D-Rex, a program for calculation of seismic anisotropy due to crystal lattice preferred orientation in the convective upper mantle. *Geophysical Journal International*, *158*(2), 744–752.

Karato, S.-I. (1989). Grain growth kinetics in olivine aggregates. *Tectonophysics*, *168*(4), 255–273.

Karato, S.-I. (2008). Deformation of earth materials. *An Introduction to the Rheology of Solid Earth*, *463*.

Karato, S.-I., & Jung, H. (2003). Effects of pressure on high-temperature dislocation creep in olivine. *Philosophical Magazine*, *83*(3), 401–414.

Karato, S.-I., Jung, H., Katayama, I., & Skemer, P. (2008). Geodynamic significance of seismic anisotropy of the upper mantle: New insights from laboratory studies. *Annual Review of Earth and Planetary Sciences*, *36*, 59–95.

Karato, S.-I., & Wu, P. (1993). Rheology of the upper mantle: A synthesis. *Science*, *260*(5109), 771–778.

Karato, S.-I., Zhang, S., & Wenk, H.-R. (1995). Superplasticity in Earth's lower mantle: Evidence from seismic anisotropy and rock physics. *Science*, *270*(5235), 458–461.

Kneller, E. A., Van Keken, P. E., Karato, S.-I., & Park, J. (2005). B-type olivine fabric in the mantle wedge: Insights from high-resolution non-Newtonian subduction zone models. *Earth and Planetary Science Letters*, *237*(3–4), 781–797.

Korenaga, J., & Jordan, T. H. (2003). Physics of multiscale convection in Earth's mantle: Onset of sublithospheric convection. *Journal of Geophysical Research*, *108*(B7), 2333. https://doi.org/10.1029/2002JB001760

Lallemant, H. G. A., Mercier, J. C. C., Carter, N. L., & Ross, J. V. (1980). Rheology of the upper mantle: Inferences from peridotite xenoliths. *Tectonophysics*, *70*(1–2), 85–113.

Lee, C.-K., Han, S.-C., & Steinberger, B. (2011). Influence of variable uncertainties in seismic tomography models on constraining mantle viscosity from geoid observations. *Physics of the Earth and Planetary Interiors*, *184*(1–2), 51–62.

Li, D., Gurnis, M., & Stadler, G. (2017). Towards adjoint-based inversion of time-dependent mantle convection with nonlinear viscosity. *Geophysical Journal International*, *209*(1), 86–105.
Masuti, S., Karato, S.-I., Girard, J., & Barbot, S. D. (2019). Anisotropic high-temperature creep in hydrous olivine single crystals and its geodynamic implications. *Physics of the Earth and Planetary Interiors*, *290*, 1–9.
Moulik, P., & Ekström, G. (2014). An anisotropic shear velocity model of the Earth's mantle using normal modes, body waves, surface waves and long-period waveforms. *Geophysical Journal International*, *199*(3), 1713–1738.
Müller, R. D., Sdrolias, M., Gaina, C., & Roest, W. R. (2008). Age, spreading rates, and spreading asymmetry of the world's ocean crust. *Geochemistry, Geophysics, Geosystems*, *9*, Q04006. https://doi.org/10.1029/2007GC001743
Mullet, B. G., Korenaga, J., & Karato, S.-I. (2015). Markov chain Monte Carlo inversion for the rheology of olivine single crystals. *Journal of Geophysical Research: Solid Earth*, *120*, 3142–3172. https://doi.org/10.1002/2014JB011845
Nicolas, A., & Christensen, N. I. (1987). Formation of anisotropy in upper mantle peridotites—A review. *Composition, Structure and Dynamics of the Lithosphere-Asthenosphere System*, *16*, (pp. 111–123).
Panning, M. P., Lekić, V., & Romanowicz, B. A. (2010). Importance of crustal corrections in the development of a new global model of radial anisotropy. *Journal of Geophysical Research*, *115*, B12325. https://doi.org/10.1029/2010JB007520
Podolefsky, N. S., Zhong, S., & McNamara, A. K. (2004). The anisotropic and rheological structure of the oceanic upper mantle from a simple model of plate shear. *Geophysical Journal International*, *158*(1), 287–296.
Press, W. H., Teukolsky, S. A., Vetterling, W. T., & Flannery, B. P. (2007). *Numerical recipes 3rd edition: The art of scientific computing* (3rd ed.). Cambridge University Press.
Ratnaswamy, V., Stadler, G., & Gurnis, M. (2015). Adjoint-based estimation of plate coupling in a non-linear mantle flow model: theory and examples. *Geophysical Journal International*, *202*(2), 768–786.
Rose, I. R., & Korenaga, J. (2011). Mantle rheology and the scaling of bending dissipation in plate tectonics. *Journal of Geophysical Research*, *116*, B06404. https://doi.org/10.1029/2010JB008004
Rubinstein, R. Y. (1981). *Simulation and the Monte Carlo method*. New York, NY, USA: John Wiley & Sons. Inc.
Spiegelman, M., & McKenzie, D. (1987). Simple 2-D models for melt extraction at mid-ocean ridges and island arcs. *Earth and Planetary Science Letters*, *83*(1–4), 137–152.
Stadler, G., Gurnis, M., Burstedde, C., Wilcox, L. C., Alisic, L., & Ghattas, O. (2010). The dynamics of plate tectonics and mantle flow: From local to global scales. *Science*, *329*(5995), 1033–1038.
Steinberger, B., Sutherland, R., & O'connell, R. J. (2004). Prediction of Emperor-Hawaii seamount locations from a revised model of global plate motion and mantle flow. *Nature*, *430*(6996), 167–173.
Uyeda, S., & Kanamori, H. (1979). Back-arc opening and the mode of subduction. *Journal of Geophysical Research*, *84*(B3), 1049–1061.
van Hunen, J., Zhong, S., Shapiro, N. M., & Ritzwoller, M. H. (2005). New evidence for dislocation creep from 3-D geodynamic modeling of the pacific upper mantle structure. *Earth and Planetary Science Letters*, *238*(1–2), 146–155.
Van der Wal, D., Chopra, P., Drury, M., & Gerald, J. F. (1993). Relationships between dynamically recrystallized grain size and deformation conditions in experimentally deformed olivine rocks. *Geophysical Research Letters*, *20*(14), 1479–1482.
Watts, A. B., & Zhong, S. (2000). Observations of flexure and the rheology of oceanic lithosphere. *Geophysical Journal International*, *142*(3), 855–875.
Worthen, J., Stadler, G., Petra, N., Gurnis, M., & Ghattas, O. (2014). Towards adjoint-based inversion for rheological parameters in nonlinear viscous mantle flow. *Physics of the Earth and Planetary Interiors*, *234*, 23–34.
Yang, T., & Gurnis, M. (2016). Dynamic topography, gravity and the role of lateral viscosity variations from inversion of global mantle flow. *Geophysical Supplements to the Monthly Notices of the Royal Astronomical Society*, *207*(2), 1186–1202.
Zhong, S., & Gurnis, M. (1996). Interaction of weak faults and non-Newtonian rheology produces plate tectonics in a 3D model of mantle flow. *Nature*, *383*(6597), 245–247.